Analysis of the electrical double layer using electrochemical X-ray photoelectron spectroscopy

Louisia, S.; Eggebeen, J.J.J.; Adnan, A.; Deka, N.; Kam, L.B.T. de; Kolmeijer, K.E.; ... ; Mom, R.V.

Electrochimica Acta 572 (2026) 149132

Contents lists available at ScienceDirect

Electrochimica Acta

journal homepage: www.journals.elsevier.com/electrochimica-acta

Analysis of the electrical double layer using electrochemical X-ray photoelectron spectroscopy

Sheena Louisia [a,b,*], Jordy J.J. Eggebeen [a], Ariba Adnan [a], Nipon Deka [a,d], Lucas B.T. de Kam [a], Kees E. Kolmeijer [a], Nicci L. Fröhlich [a], Rick S. Kort [a], Katharina Doblhoff-Dier [a], Ethan J. Crumlin [c], Marc T.M. Koper [a], Rik V. Mom [a]

[a] Leiden Institute of Chemistry, Leiden University, Leiden 2300 RA, The Netherlands
[b] Sorbonne Université, CNRS, Laboratoire Interfaces et Systèmes Électrochimiques (LISE), F-75005 Paris, France
[c] Chemical Sciences Division and Advanced Light Source, Lawrence Berkeley National Laboratory, Berkeley, California 94720, United States
[d] PSI Center for Energy & Environmental Science, Paul Scherrer Institute, 5232 Villigen PSI, Switzerland

ARTICLE INFO

Keywords:
EC-XPS
Double layer
Dip-and-pull

ABSTRACT

The element-sensitivity of X-ray spectroscopies offers the potential to disentangle the individual chemistries of water, ions, and adsorbates at the electrode-electrolyte interface in an element-by-element manner. However, targeted experimental design is needed to establish interface-sensitive in situ X-ray spectroscopy in a realistic electrochemical environment. Here, we demonstrate how electrochemical X-ray photoelectron spectroscopy (EC-XPS) in the dip-and-pull geometry can be used to specifically probe the behavior of ions in the electrical double layer. Taking the case study of a polycrystalline Au foil in 50 mM $KClO_4$ electrolyte, we tracked the electrochemical response of interfacial K^+ cations across a broad potential range. We show how, in combination with modeling, key parameters such as the potential of zero charge (PZC), ion packing behavior, dielectric saturation, and the electrostatic potential decay in the double layer can be extracted from the data. Importantly, we also analyze how the experimental conditions and non-idealities can influence the results and put forward criteria for reliable experimentation and data analysis.

1. Introduction

The chemistry that takes place at the electrode-electrolyte interface is at the heart of both charge storage and electrocatalytic processes. Consequently, methodologies capable of probing this interfacial chemistry are instrumental for advancing our understanding and engineering capabilities of electrochemical systems. A major current challenge in such characterization is resolving the properties of the interfacial electrolyte, i.e. the electrical double layer (EDL). This limitation is particularly significant because the interfacial solvent molecules and ions play a central role in the electrochemistry of numerous systems [1–3]. To take full advantage of these electrolyte effects, it is critical to understand what interfacial electrolyte structure is formed and how it is related to the composition of the bulk electrolyte, motivating continued development of spectroscopic [4] and [5] microscopic tools that can deliver such insight.

Properties that are high on the "wish list" for an EDL characterization technique are 1) a high interface sensitivity with respect to the bulk electrode and electrolyte, 2) the capability to individually track the chemistries of the interfacial solvent, cations *and* anions, and 3) the capability to quantify interfacial ion concentrations. A promising technique to fulfill this list is electrochemical X-ray photoelectron spectroscopy (EC-XPS). XPS traditionally requires ultra-high vacuum, making it inherently incompatible with the study of solid-liquid interfaces. However, the development of differentially pumped X-ray sources and electron analyzers, combined with tailored spectro-electrochemical cell design, has opened up the way to interface the vacuum required for XPS with aqueous electrochemical environments. The key attraction of this EC-XPS approach is that it facilitates analysis of the electrode-electrolyte interface in an element-by-element manner. For example, the Pt|0.1 M KOH interface can be characterized using the Pt 4f core level for the electrode surface, the K 2p core level for the K^+ ions, and the O 1s core level for the water molecules and oxygenated adsorbates [6]. In this way, EC-XPS has been used, amongst others, to

* Corresponding author.
E-mail address: sheena.louisia@sorbonne-universite.fr (S. Louisia).

https://doi.org/10.1016/j.electacta.2026.149132
Received 2 March 2026; Received in revised form 15 May 2026; Accepted 17 May 2026
Available online 17 May 2026

analyze the dynamic surface composition of alloys [7], to resolve the potential profile of the EDL [8], to identify adsorbed catalytic intermediates [9], and to track surface redox chemistry [6,7,10–12].

Here, we further extend the use of EC-XPS to analyze the concentration and electrostatic potential of ions in the EDL. Using the dip-and-pull EC-XPS approach, we analyze the case study of K^+-Au interactions at the Au|50 mM $KClO_4$ interface. This interface is chosen specifically because of its broad double-layer-dominated potential range without interference from faradaic processes or specific adsorption. The analysis is backed by Poisson-Boltzmann modeling and *ab initio* molecular dynamics simulations, providing a thorough evaluation of what insights can be reliably extracted from the EC-XPS data. Apart from showing the proof-of-concept of using EC-XPS to analyze interfacial ion concentrations and potentials, we provide a technical guide on how to carefully perform the measurements, how to assess the reliability of the data, and which information can be gathered from its analysis.

2. Methods

2.1. Materials

The 50 mM $KClO_4$ electrolyte was prepared using MilliQ water (DI, ρ=18.2 MΩ cm) and $KClO_4$ (99.99%, Aldrich). For the working and counter electrode, we used a 0.5 mm thick Au foil (0.7 cm x 3 cm, 99.995%, Mateck) and a 0.5 mm diameter Au wire (99.99%, Mateck), respectively. A 0.5 mm diameter Pt wire (99.99%) was used as a pseudo-reference electrode (RE). Note that a pseudo-RE electrode was used here because vacuum-compatible Ag/AgCl electrodes displayed Cl^- leakage, causing XPS-observable chloride contamination in the double layer (**Fig. S1**). The Au foil working electrode was mechanically roughened with sandpaper and cleaned along with the glassware used for all experiments. In the cleaning procedure, they were stored in an oxidizing 1 g/L $KMnO_4$ solution acidified with ~1 mM H_2SO_4 (95–97%, for analysis, Emsure). The storage solution was poured out and rinsed before adding a dilute solution of piranha. After 20–30 min, the dilute piranha was discarded and the glassware rinsed with ultrapure water. The glassware was then sequentially boiled 5 times in ultrapure water.

2.2. EC-XPS measurements

The EC-XPS experiments were carried out using the "dip-and-pull" method at beamline 9.3.1 of the Advanced Light Source, Berkeley, United States [13]. In this method, a 150 mL glass beaker filled to the rim with electrolyte is placed on a motorized stage inside the XPS measurement chamber. The cleaned working, counter, and reference electrodes are mounted on a separate manipulator (Fig. 1 **and S2**), enabling free movement of the electrodes with respect to the beaker and the electron analyzer. For the measurement, the electrodes are dipped into the electrolyte and then pulled up to establish a thin electrolyte film on the working electrode, through which the XPS measurements are conducted.

Prior to loading the electrolyte into the chamber, it was degassed thoroughly in a vacuum chamber. To limit the rate of evaporation from electrolyte once placed in the XPS vacuum system, an additional small beaker of degassed water was also placed inside the XPS chamber. The chamber was pumped down slowly to minimize the risk of bubble nucleation from gases still trapped inside the electrolyte. Once the chamber pressure drops below 20 mbar, the electrode holder was moved to align the working electrode (WE) with the beam. Throughout the experiment, the chamber pressure was maintained at roughly the water vapor pressure (~20 mbar) to ensure that the electrolyte does not become more concentrated over time due to evaporation, especially in the electrolyte film at the measurement spot.

To minimize the distance between the wetted WE and the analyzer nozzle, while ensuring the measurement of a stable wet electrolyte film, the edge of the beaker was placed as close as possible to the analyzer nozzle while the WE was placed as close as possible to the edge of the beaker facing the nozzle. In this configuration, the Au foil WE was dipped about 2–3 cm into the beaker containing the prepared electrolyte. After performing several cyclic voltammograms (CVs) between −1.0 V and 0.6 V vs. Pt pseudo-RE to ensure the proper electrochemical response of the WE, a potential was held. Under potential control, the WE was pulled about 1 cm out of the electrolyte for every EC-XPS measurement. The identification of a "wet film" was determined when the Au 4f counts dropped by an order of magnitude during this "pull" step. The focus was re-determined using the Au 4f counts before measuring other elements. Once a wet film was identified, a O 1s scan was measured. The electrochemical connectivity of the film was determined by tracking the O 1s peak positions when the applied potential was changed. When the O 1s peak position shifts ~−1 eV for every 1 V, K 2p was measured (**Table S1** and **Fig. S3**). The BE shift reversibility of the O 1s was also verified to rule out any time-dependent effect (**Fig. S4**). C 1s was also measured to ascertain the contribution of adventitious carbon in the system and was found to be minimal with a distinctly lower potential-dependence than the other electrolytic species, i.e., H_2O and K^+ (**Fig. S5**). A Au 4f spectrum was recorded before and after each series of spectra to track changes in the electrolyte film thickness (**Fig. S3**). A 4 keV X-ray was used and the pass energy was set to 100 eV for all measurements. An energy step of 0.1 eV and step time of 250 ms were used for all measurements used for peak integration. O 1s, Au 4f, and K 2p were obtained in 1, 3, and 20 sweeps, respectively. No apparent oxidation of the Au foil was observed in the studied potential range (**Fig. S6**).

Given the long exposure to a focused X-ray beam in the experiments, consideration was given to possible beam-induced effects due to, e.g. water radiolysis [14]. However, while several works have reported clear beam-induced changes in their system [14–16], we did not observe a noticeable BE or peak width change for the O 1s, Cl 2p, or Au 4f signals measured before and after 1–2 h at the same spot. Only a change in relative intensity for O 1s and Au 4f, which we associate with the thinning of the electrolyte film, could be clearly observed (**Fig. S3**). Although ClO_4^- degradation into Cl^- could have been expected under beam exposure, neither the Cl 2p (**Fig. S7**) nor the CV of the system suggests any significant Cl^- accumulation, which, in the presence of Au at more positive potentials, is expected to adsorb strongly. Therefore, we consider that within the scope of our measurements, the beam-induced effects, although likely present, do not significantly perturb the measured Au|50 mM $KClO_4$ EDL.

2.3. Electrochemistry

All electrochemical measurements were managed using a Biologic SP-300 potentiostat. Once the electrodes were submerged in the degassed electrolyte, several cyclic voltammograms (CV) were collected to check the electrochemistry of the Au foil. Although degassed, the first few CVs exhibit reductive currents, a signature of the presence of O_2. The O_2 reducing currents eventually subsided, leaving a broad double layer region typical of Au. The potential measured against the Pt pseudo-RE was calibrated by comparing the CVs to those recorded on polycrystalline Au in 50 mM $KClO_4$ in our home lab using a reversible hydrogen electrode (RHE) Hydroflex (Gaskatel). In the measured potential range of −1.0 to 0.6 V vs Pt pseudo-RE, we observe a shift of approximately 0.72 V between the potential vs Pt and the potential vs RHE. It's worth noting that the correspondence between the pseudo-RE and the RHE potential windows is approximate because the chemical stability of Pt as a pseudo-RE can fluctuate, especially at the lower/upper potential bounds. To ensure experimental consistency, the CV was regularly measured in between each set of dip-and-pull XPS scans to track the stability of the pseudo-RE. Regular CVs also helped track possible contaminant accumulation.

2.4. SESSA modeling

Signal attenuation due to photoelectron scattering was modeled using the SESSA 2.2.2 simulation package [17]. The model was constructed with an Au substrate of infinite depth, covered with a 1 nm film of 2 M K^+ ions in water and a bulk 50 mM K^+ in water film of varying thickness (4–36 nm). Input parameters are the atomic densities of H, O, K, and Au in the layers, the bandgap of each layer (0 eV for Au, 6.9 eV for the water-based layers), and the surface roughness of the Au substrate (relative surface area = 0 for simulations on the flat surface and relative surface area = 2.2 for the rough surface). SESSA uses the TPP-2 M formula to calculate the inelastic mean free path and the scattering cross sections of photoelectrons based on these parameters. Using those parameters, a large number of photoelectron trajectories are generated to determine the expected intensities of XPS signals for different core levels (**Text S1**).

2.5. Modified Poisson-Boltzmann model

The continuum model of the EDL consists of a modified Poisson-Boltzmann equation with appropriate boundary conditions. Both are outlined below.

The modified Poisson-Boltzmann equation, including finite ion size effects and dielectric saturation, was previously derived by Abrashkin et al. [18] and Gongadze and Iglič [19,20]. For a univalent electrolyte, it can be written in terms of dimensionless variables $\bar{x} = x/\Lambda$ with $\Lambda = 1$ Å and the potential relative to the bulk electrolyte $\bar{\phi} = \beta e \phi$, as

$$\nabla(\varepsilon \nabla \bar{\phi}) = -\kappa(n_c - n_a)$$

Bars here denote dimensionless variables and $\kappa = \beta e^2 (\Lambda \varepsilon_0)^{-1}$. The relative permittivity ε depends on the local electric field $-\nabla\bar{\phi}$ via

$$\varepsilon = \varepsilon_{\min} + \kappa p^2 \bar{n}_s \frac{\mathscr{L}(p\nabla\bar{\phi})}{p\nabla\bar{\phi}}$$

where $\varepsilon_{\min}$ is the relative permittivity at strong electric fields, $\mathscr{L}(x)$ is the Langevin function, and the dimensionless effective dipole of water $p \approx 0.99$ is set such that $\varepsilon \approx 78.4$ when $\nabla\bar{\phi} \to 0$. In correspondence with traditional double layer models [21], $\varepsilon_{\min} = 5$ is chosen.

To model excluded volume effects, the dimensionless cation, anion, and solvent bulk number densities $\bar{n}_c$, $\bar{n}_a$, and $\bar{n}_s$ are written as

$$\bar{n}_i = \bar{n}_{\max} \frac{\bar{n}_i^{\text{bulk}} \Theta_i}{\sum_{i=a,c,s} \gamma_i \bar{n}_i^{\text{bulk}} \Theta_i}$$

where γ_i denotes the number of lattice sites occupied by a single particle of species i, and $\bar{n}_{\max} = 0.0333$ is the lattice site density, which is chosen such that bulk water has a density of $n_s = 55$ M when $\gamma_s = 1$. The Boltzmann factors Θ_i are given by

$$\Theta_c = \exp - \bar{\phi}$$

$$\Theta_a = \exp \bar{\phi}$$

$$\Theta_s = \frac{\sinh p\nabla\bar{\phi}}{p\nabla\bar{\phi}}.$$

For the ions, values of $\gamma_c = 5$ and $\gamma_a = 2$ are chosen, respectively, slightly smaller than the bulk hydrated ion sizes used in the implementation of Zhen et al. [22] to account for desolvation in the double layer.

The model is solved for an infinite planar electrode. The potential at the right boundary (water-air interface) is set to $\phi = 0$. The left boundary is set at the plane of closest approach for electrolyte ions (outer Helmholtz plane, OHP), a distance of δ_{OHP} from the working electrode. Requiring continuity of the electric displacement and assuming that the permittivity is continuous across the OHP,

$$\bar{\phi}_{\text{OHP}} - \bar{\phi}_0 = (\nabla\bar{\phi})_{\text{OHP}} \delta_{\text{OHP}}$$

where ϕ_0 is the potential at the electrode. The polarization of interfacial water is included only through the field-dependent permittivity function, corresponding to a simplification of the model of Zhen et al. [22], who include interfacial water in the boundary condition explicitly. Based on the molecular dynamics simulations by Guo et al. [23], a value of $\delta_{\text{OHP}} = 4$ Å is chosen.

An overview of model parameters is given in **Table S4**. The ion concentration is fixed to the experimental one. The chosen model parameters allow for a reasonable representation of the double layer capacitance (see **Fig. S9**). The numerical implementation is available online, see [24].

The signal intensity from the K 2p state is predicted from the ion concentration $c(z)$, obtained from the modified Poisson-Boltzmann model, using the straight-line attenuation model:

$$I \propto \int_0^L c(z)\, e^{-(L-z)/\lambda} dz,$$

where z is the distance from the surface, L the thickness of the water layer, and λ is the attenuation length. The experimental data and SESSA simulations were used to set L and λ. $L = 12.8$ nm was determined based on the average value from the measurements for the 3 most positive potentials, and $\lambda = 4.52$ nm is determined from a fit of the K 2p attenuation versus film thickness in the SESSA model over the film thickness range of 0–19 nm.

To predict the peak-shift of the K 2p signal, we assume that the shift in binding energy of an ion residing at position z is determined only by the mean-field potential $\phi(z)$. The expected peak shift is obtained by binning the potential energies $e(\phi(z) - \phi_0)$ in a histogram, weighted by the local ion concentration $c(z)$ and attenuation factor $\exp[-(L-z)/\lambda]$. Shifting the potentials by ϕ_0 is necessary to simulate the experimental setup, in which the working electrode is grounded.

2.6. Ab initio molecular dynamics

Ab initio molecular dynamics (AIMD) simulations were used to investigate the electronic energy levels of the K^+ ions at the Au(111)/electrolyte interface.

Our models consist of a 6 × 6 atom slab with six layers and an optimized lattice constant of 4.216 Å, in close agreement with the experimental value for gold (4.08 Å) [25]. An electrolyte consisting of 215 water molecules and either no (PZC) or 4 K^+ cations was placed above the interface, leading to a water thickness of around 25 Å. To prevent interaction between the periodic images normal to the interface, an additional 20 Å of vacuum was added, leading to a final cell dimension of 17.887 × 15.491 × 59.671 $Å^3$ (see **Fig. S10**).

All calculations were carried out with the CP2K Quickstep code [26], which uses the Gaussian and plane wave (GPW) approach to compute electronic structure efficiently. Core electrons were modeled with Goedecker, Teter, and Hutter (GTH) pseudopotentials [27]. Valence states were described with a double zeta basis including one set of polarization functions (DZVP). For O, H, Au, and K we used the standard DZVP-MOLOPT-SR-GTH basis set together with the GTH-PBE pseudopotentials q6 (O), q1 (H), q11 (Au), and q9 (K). Exchange and correlation were described using the revised Perdew-Burke-Ernzerhof (RPBE) functional [28], and dispersion interactions were included via the Grimme D3 correction [29]. The plane wave cutoff was 500 Ry for AIMD and 800 Ry for single point calculations. AIMD was performed using second-generation Car-Parrinello molecular dynamics (SGCPMD) [30]. A Langevin thermostat maintained the system at 320 K [31]. We applied a global friction coefficient $\gamma_L = 0.001$ fs^{-1} [32]. Region dependent intrinsic friction coefficients γ_D were used, with a value of 5.0×10^{-5} fs^{-1} for the mobile Au atoms, which was found to be similar to that of Pt

[32], and 1.0×10^{-4} fs^{-1} for the electrolyte species (water and K^+), determined by equilibration tests. Brillouin zone sampling was restricted to the Γ point. The four bottom Au layers were held fixed at bulk positions, whereas the two upper layers evolved dynamically.

Starting structures for AIMD were generated from 5 ns of classical molecular dynamics. Water, Au, and K were described with TIP3P [33], Heinz 2008 [34], and Joung 2008 [35] force fields, respectively. The classical MD equilibration was followed by AIMD to further equilibrate the system for approximately 5 ps. Subsequently, 13.5 ps of AIMD were used for analysis in the presence of K^+ ions, while 5 ps were used for the Au-water system. All AIMD simulations employed a 0.5 fs time step to properly resolve O H vibrational motion [32].

To follow the electronic structure along with the trajectories, single point calculations were carried out every 50 fs. Self-consistent field convergence was set to 3.0×10^{-7} Hartree, with up to 500 SCF iterations allowed per snapshot to ensure robust convergence. Electronic occupations were handled using Fermi-Dirac smearing at an electronic temperature of 300 K. Electrode potentials were obtained for each single point calculation using the computational standard hydrogen electrode (cSHE) approach [36]. The potential difference between our 4 ion calculation to our 0 ion calculation is −1.26 V.

To obtain the binding energy shift, the projected density of states (PDOS) of each K^+ ion was computed for every snapshot and referenced to the Fermi level of the snapshot in question. The ion-surface distances Δz were extracted as the distance between the ion z coordinate and the mean z coordinate of the topmost Au layer. Since the core levels are not accessible in pseudopotential calculations, the PDOS-weighted mean energies were computed for the 3 s and 3p PDOS. We take the peak of the 3 s PDOS as representative of the core level binding energy. By plotting peak-averaged PDOS energy as a function of ion-surface distance Δz, one can visualize trends for the shifts of the 3 s level binding energy.

3. Results and discussion

The electrochemical interface formed between a polycrystalline Au foil and a 50 mM $KClO_4$ electrolyte was studied using EC-XPS. This system was chosen to minimize chemical interactions over the widest possible potential range, so that the EDL is the only potential-dependent aspect of the system. In the case of Au, the adsorbate-free region is typically found between 0 and 1.0 V vs RHE, where its potential of zero charge (PZC) also lies. At pH 7, the latter is expected to span between 0.6 and 0.9 V vs RHE, depending on the facets of the Au surface [37,38]. Among the anions, ClO_4^- is considered non-specifically adsorbing on Au. Without specific adsorption, we can investigate the potential-dependent response of the ions where the charging of the double layer is the principal electrochemical event. In this work, the ion distribution in the EDL is monitored below and within the region of PZC.

The measurement first requires that the electrodes are dipped in the

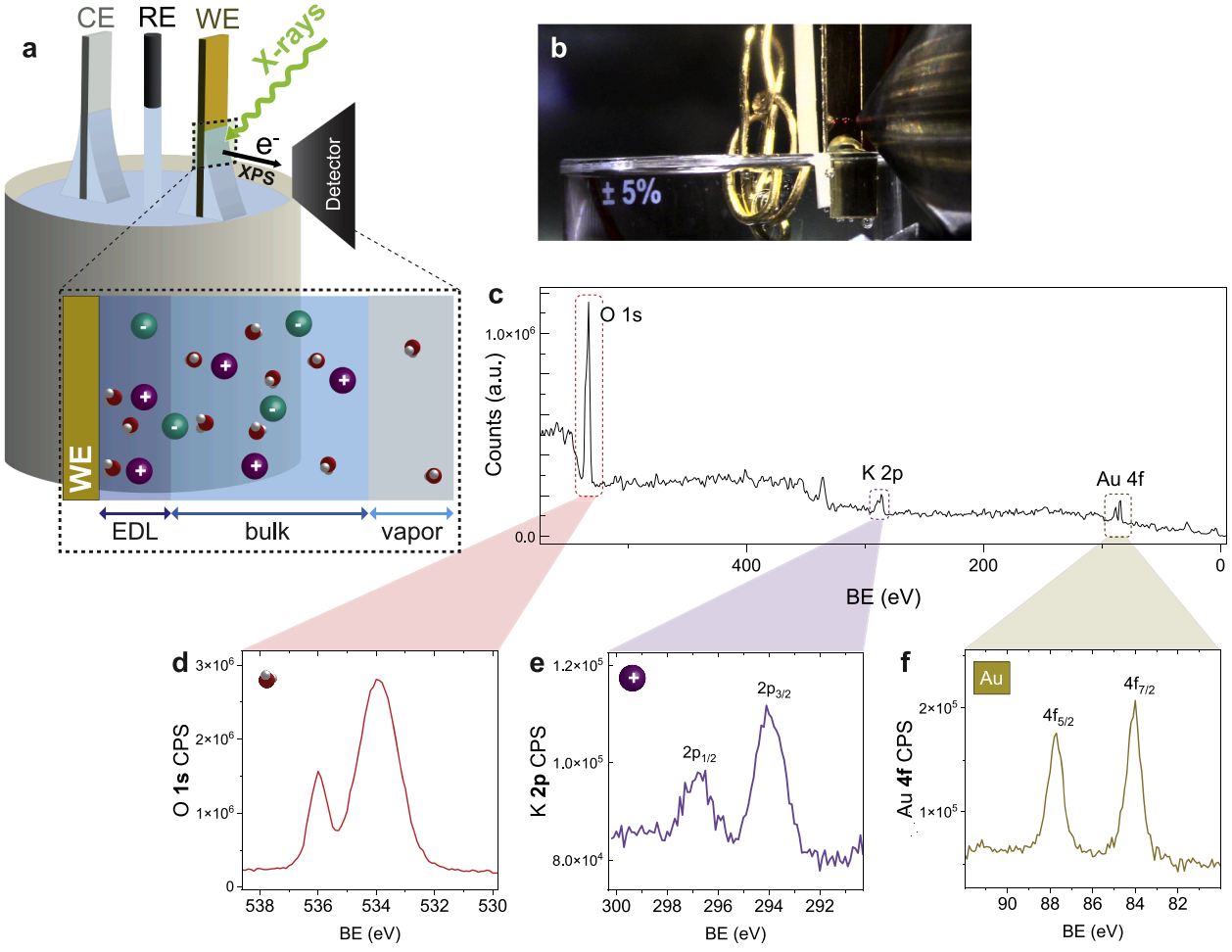

Fig. 1. Chemical overview of an electrochemical interface through EC-XPS. (**a**) Schematic of the dip-and-pull geometry for XPS measurements. WE, CE, and RE denote the working, counter, and reference electrode, respectively. The inset shows the 10–40 nm electrolyte film on the WE that is probed by the XPS, with the electrical double layer noted as EDL (**b**) Photo of the dip-and-pull setup. (**c**) Survey spectrum of the Au-$KClO_4$ interface showing peaks of varying intensities related to ions (K 2p, Cl 2p), water (O 1s), and the electrode surface (Au 4f) at −0.1 V vs RHE. (**e-f**) Show high-resolution spectra of these core levels. All spectra were acquired with an X-ray energy of 4 keV.

electrolyte and then pulled up to form the thin electrolyte film necessary to measure the elements present at the interface (Fig. 1a–b). The film can be formed and remains stable in the vacuum chamber for at least 1 hour and up to 2 h because the chamber pressure is held at water vapor pressure, ~20 mbar. The elemental sensitivity of the method allows us to separately track the chemistry of the different components coexisting at the formed interface (Fig. 1c). From this measurement, we seek to simultaneously obtain information about the water via O 1s spectra (529–539 eV) (Fig. 1d), K^+ ions via K 2p spectra (291–300 eV) (Fig. 1e), and ClO_4^- ions via Cl 2p (194–204 eV) spectra, the latter which was not detected (**Fig. S7**). Finally, we can track the Au 4f (80–92 eV) signal (Fig.1f) to probe the electrode surface, completing the overview of all of the interface components.

A critical factor in the measurements is the electrolyte film thickness on the electrode at the focal point. It should be thick enough to form a complete electrical double layer, but thin enough to facilitate photoelectrons generated at the electrode-electrolyte interface to reach the electron analyzer. These conditions are generally met when the film thickness is 10–40 nm over the entire probed area. This stringent requirement is one of the main challenges of the dip-and-pull method. To monitor if this requirement is met, the electrolyte film thickness L can be determined from the attenuation of the Au 4f signal (Fig. 2c), or the ratio between the liquid (H_2O_{liq}) and gaseous water (H_2O_{gas}) O 1s peak (Fig. 2a; b). Because the Au 4f attenuation responds significantly more strongly to the electrolyte film thickness, we focus on the Au 4f attenuation method here. The attenuation of the signal intensity should stem principally from photoelectron scattering in the electrolyte film, which becomes stronger (more attenuation) for thicker electrolyte films. Most commonly, this attenuation is modeled using the straight-line approximation:

$$I = I_0 e^{-L/\lambda} \quad (1)$$

where the signal intensity I is related to the signal intensity of the dry surface I_0 (in 20 mbar H_2O vapor) and the inelastic mean free path (IMFP) λ of the Au 4f photoelectrons through the electrolyte film (**Text S2**). Using 11.45 nm as the IMFP of liquid water [39] and the experimental I/I_0 ratios, a film thickness range of 28–40 nm is obtained for our experimental conditions.

However, several factors are not considered in this simple model. First, it does not consider the presence of the K^+ ions in the electrolyte film. Secondly, it does not weigh in the effect of surface roughness, which was purposely increased in this study to promote wetting. The roughness is known to have a big impact on the signal attenuation as it increases the average path length that electrons must travel through the electrolyte, overall diminishing the signal intensity [40–42]. To acknowledge the impact of these factors, along with any (usually small) elastic scattering effects, we conducted a simulation of electron spectra for surface analysis (SESSA) for the Au 4f attenuation as a function of the electrolyte film thickness. When comparing these SESSA simulations to

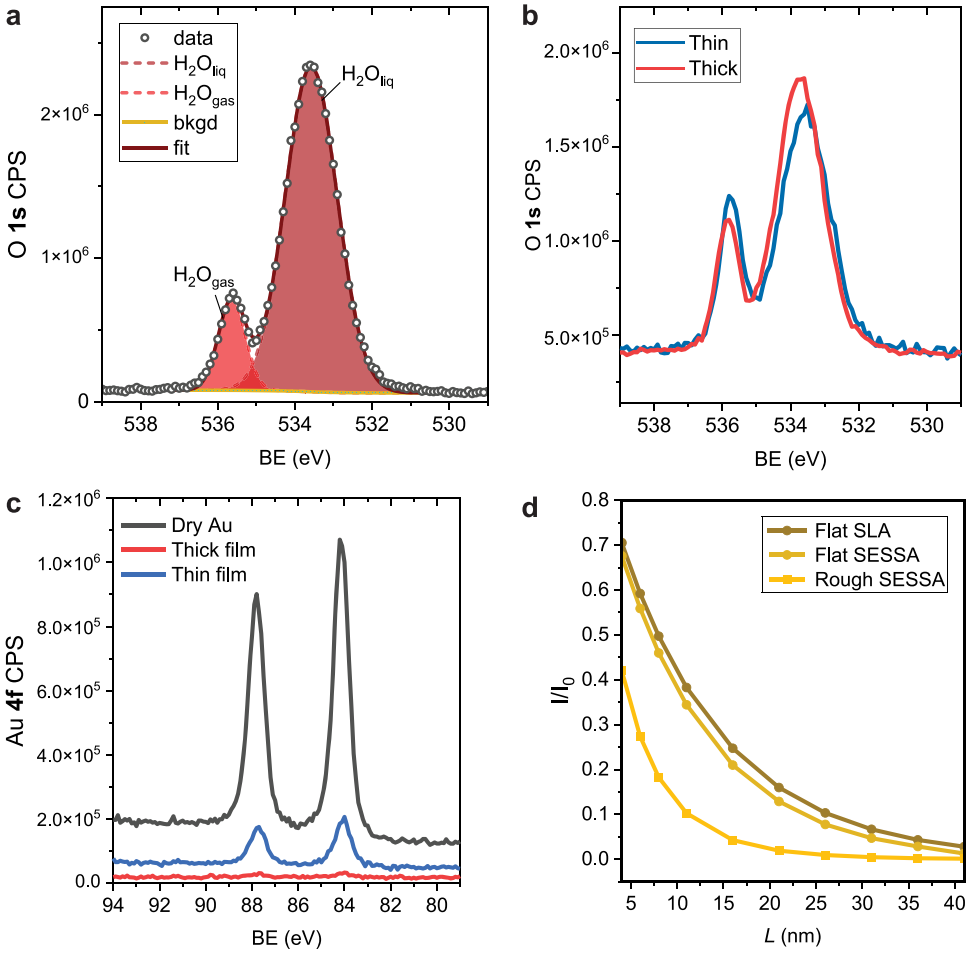

Fig. 2. Monitoring electrolyte film formation during dip-and-pull XPS. (**a**) O 1s spectra features two distinct peaks for gaseous water (H_2O_{gas}) at ca. 536 eV and liquid water (H_2O_{liq}) at ca. 533.5 eV. A Shirley background (bkgd) was used to integrate the respective H_2O_{liq} and H_2O_{gas} peaks. (**b**) The relative peak height ratio between H_2O_{gas} and H_2O_{liq} is sensitive to the electrolyte film thickness. (**c**) The Au 4f attenuation varies with the electrolyte film thickness. (**d**) Simulation of electron spectra for surface analysis (SESSA) of Au 4f I/I_0 as a function of electrolyte film thickness L shows a greater attenuation for a rough (square) compared to a flat (circle) surface, simulated either with a straight-line approximation (SLA) or SESSA.

the results from the straight line approximation (Fig. 2d), it can be observed that while the effect of K^+ is modest, surface roughness is a critical factor to consider for estimating the correct electrolyte film thickness. Assuming a high surface roughness (relative surface area = 2.2), we obtain a film thickness range of 12–17 nm. We consider this the lower bound estimate of the film thickness range. Overall, our analysis thus shows that the electrolyte film thickness under our experimental conditions falls within the suitable range for in situ measurements of the EDL.

In addition to measuring the electrolyte film thickness, we verified whether the measured signal originated from an electrochemically connected film and not an isolated droplet. This can be done by tracking the shift in the O 1s liquid peak with applied potential. As shown in previous works, the observed binding energy (BE) of electrolyte species varies with the potential applied to the WE [8,43]. This shift originates from the shift of the Fermi level of the electrolyte with respect to the electrode when a potential is applied (Fig. 3a). Since the WE is grounded to the electron analyzer, this means that the electrolyte Fermi level also shifts with respect to the analyzer, which directly affects the apparent BE. Hence, although the real BE (BE_{real}) of the electrolyte species may remain unchanged, the apparent BE ($BE_{apparent}$) measured by the electron analyzer will exhibit a potential dependence. This is indeed observed for the O 1s signal of water (Fig. 3b).

The $BE_{apparent}$ of O 1s is expected to shift by −1 eV for every 1 V applied. Our experiments closely match this with a slope of −0.89±0.04 eV/V (Fig. 3c) in the potential region from −0.2 to 0.7 V_{RHE}, indicating that (nearly) the entire probed area is properly electrochemically connected [44]. However, above the PZC region, the BE does not follow the expected behavior anymore (gray points). This suggests that the wetting behavior on the electrode changes above the PZC region, creating a poorly connected electrolyte film. To avoid misinterpretation of results, we therefore focus on potentials below and up to the PZC region. Electrochemically, the Au foil studied inside the XPS chamber appears to behave similarly to the polycrystalline Au foil studied in a regular glass cell purged with Ar (Fig. 3d). Measured in the same potential range, the cyclic voltammogram (CV) reveals a similar double layer-dominated potential region in both measurement conditions. Although the i-V features do not align perfectly, especially below 0.0 V_{RHE} and above 1.0 V_{RHE}, a small broad peak is observed around 0.85 V_{RHE} in both conditions. This feature is often observed for Au (111) and polycrystalline Au surfaces in non-specifically adsorbing ClO_4^- based electrolytes [45–47]. Contributing factors to the small differences between the CV in the regular and the XPS cell could come from traces of $O_{2(g)}$ in the electrolyte and uncompensated resistances induced by the electrode holder and the thin film thickness.

The analysis above verifies that our experimental conditions were suitable for probing a properly electrochemically responsive electrode-electrolyte interface. However, a critical question that remains is whether the XPS signals of ionic species mainly originate from the EDL or from the bulk part of the electrolyte film. To address this question, we used our SESSA model to compare the expected signal intensity coming from ions in the double layer and bulk electrolyte ions based on the ion concentration at the interface. We modeled the expected ion concentration profile using a modified Poisson-Boltzmann model (Fig. 4a) that

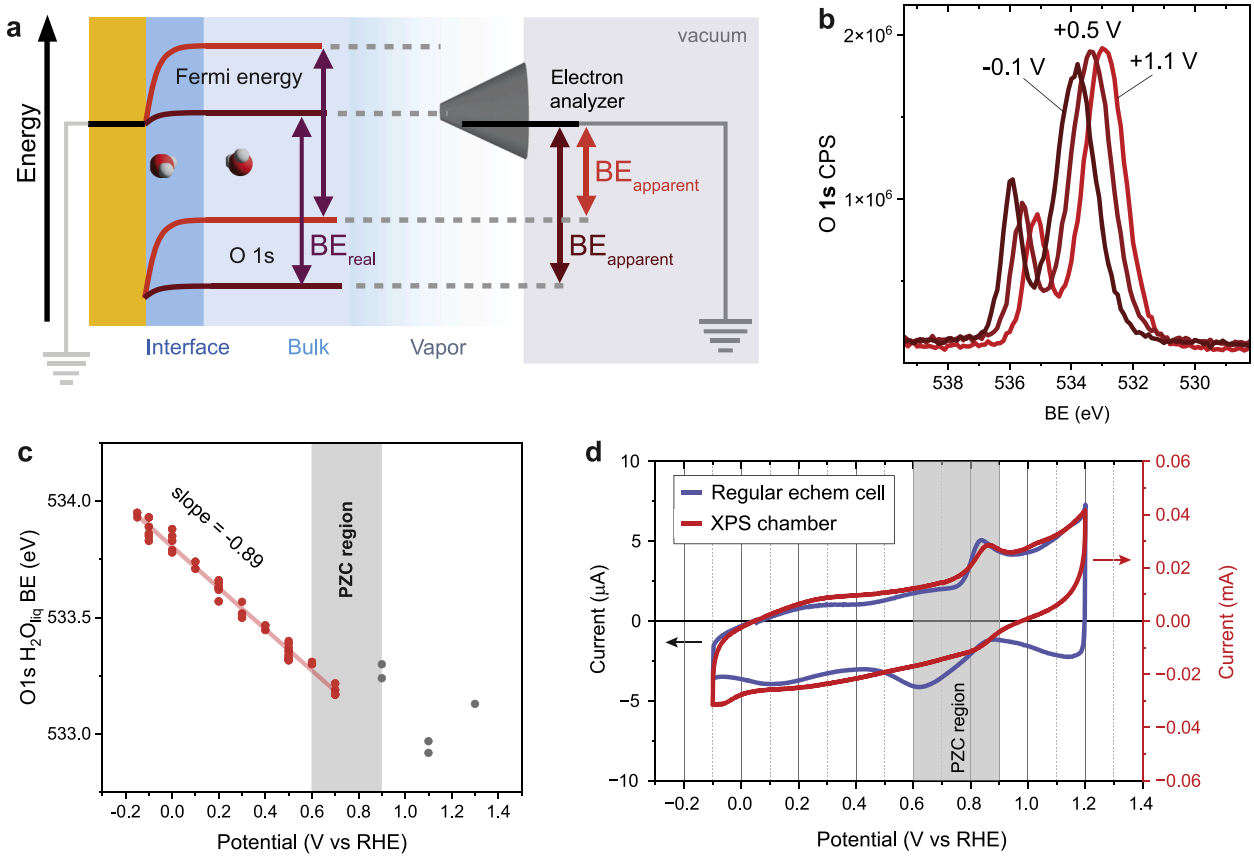

Fig. 3. Effect of potential on the binding energy of electrolyte species. **(a)** Schematic showing how the apparent BE ($BE_{apparent}$) of an electrolyte species, e.g., H_2O, changes when moving from a high (red) to a low (maroon) potential. BE_{real} denotes the real BE. The effect is shown experimentally using the O 1s spectra of water in **(b)** for three selected experiments. **(c)** Summary of measured O 1s peak position as a function of the applied potential. For experiments performed below the PZC region, a slope of −0.89±0.04 eV/V, close to the theoretical −1 eV/V is observed (red points). Above the PZC region, the expected trend is not observed (grey points). **(d)** Comparison of the cyclic voltammogram recorded in the XPS chamber (red, right y-axis) and in a regular Ar-purged glass electrochemical (echem) cell (blue, left y-axis) at a scan rate of 50 mV/s. The expected PZC region is highlighted in grey.

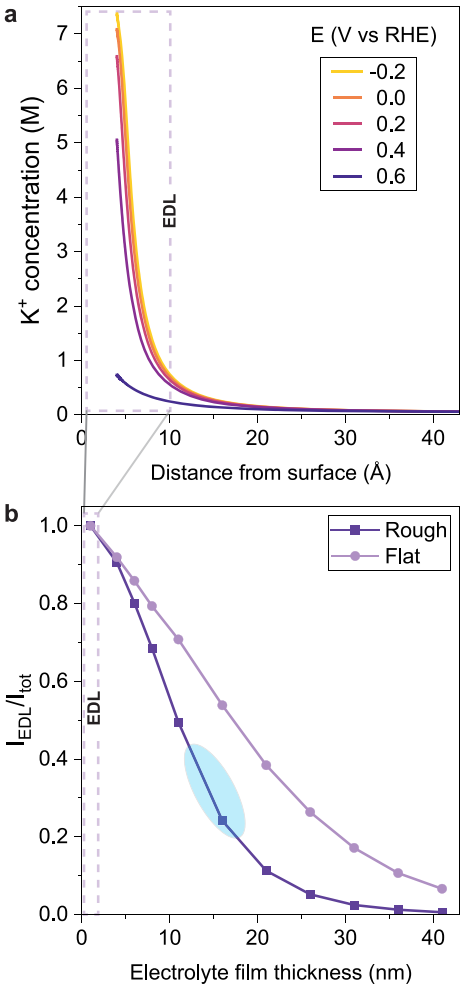

Fig. 4. Modeling of the expected bulk and surface contributions of the K 2p signal of K^+ ions at the Au-50 mM $KClO_4$ interface. (a) Simulated surface concentration of K^+ as a function of the applied potential from a modified Poisson-Boltzmann model with PZC = 0.7 V vs RHE and 50 mM K^+. **(b)** Simulated effect of surface roughness on the I_{EDL}/I_{tot} ratio of K 2p as a function of electrolyte thickness assuming EDL = 1 nm, $\langle C_{dl}\rangle$ = 2 M, and C_{bulk} = 50 mM. The difference is greater for an electrolyte film 10–20 nm thick. The experimental average film thickness region is highlighted in blue.

is parameterized in such a way as to reasonably reproduce experimental capacitance curves (see SI). For use in the SESSA model, this concentration profile is approximated by a step profile capturing the average concentration in the double layer $\langle C_{dl}\rangle$ (set as the first nm here) and in the bulk C_{bulk}.

Using this model, the fraction of double layer K 2p signal was calculated as a function of film thickness, both for the case of a flat and a rough electrode surface (Fig. 4b). For the experimental film thicknesses (12–17 nm for the more realistic rough surface, 28–40 nm for an idealized flat surface), the SESSA model predicts that a significant fraction of the signal originates from the EDL. When moving the potential from the PZC region ($\langle C_{dl}\rangle = C_{bulk}$ = 50 mM) to −0.1 V_{RHE} ($\langle C_{dl}\rangle \approx$ 2 M, C_{bulk} = 50 mM), we may expect the total K 2p signal to increase by a factor 1.25–2. Therefore, based on our modeling, one may expect that our experimental conditions are suitable for tracking the dynamic behavior of the EDL as a function of potential.

To verify our sensitivity to the double layer experimentally, we recorded K 2p and O 1s spectra as a function of potential (Fig. 5). The spectra were recorded in a random order to avoid time-dependent effects (**Fig. S11**). Upon fitting the K 2p doublet, we found most spectra yielded good residual standard deviation (**Fig. S12**). Additionally, we found that

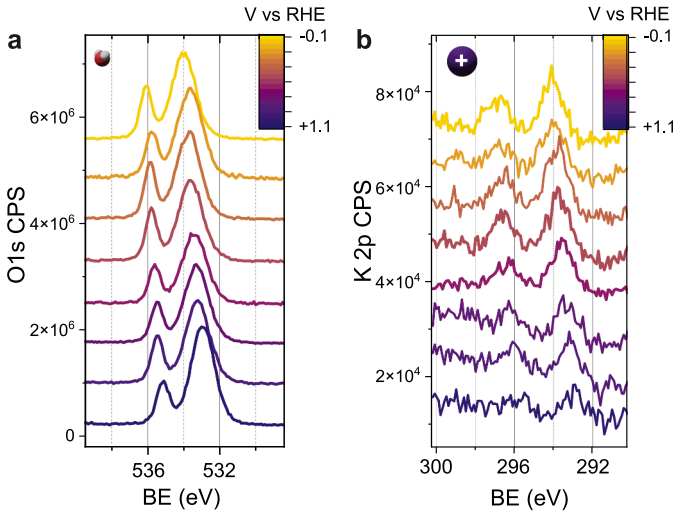

Fig. 5. Potential dependent response of electrolyte species for an Au foil in 50 mM $KClO_4$. **(a)** O 1s representative of H_2O and **(b)** K 2p representative of K^+ cations as a function of the applied potential. The absolute signal is shown (in counts per second, CPS) so that intensity changes vs. potential can be assessed.

for K 2p peaks integrated between −0.1 and 0.7 V, the signal-to-noise ratio was ~10, confirming the reliability of the data quality for further analysis (**Fig. S13**). Upon inspection of the resulting data in Fig. 5, we can see that the intensity of the bulk-dominated O 1s signal remains constant (Fig. 5a **and S14**), while the intensity of the K 2p doublet clearly exhibits a potential dependence (Fig. 5b), with more ions approaching the negatively charged electrode, as expected. The data, in fact, shows a 1.5-fold increase in signal intensity (see also Fig. 6d) when going from 0.7 V vs. RHE (expected to lie close to PZC) to −0.1 V vs. RHE, in rough agreement with the model above. Overall, this shows that the dip-and-pull EC-XPS approach can probe the potential-dependent structure of the EDL.

When analyzing the K 2p trend in more detail, it is important to consider experimental factors that could impact the K 2p intensity, such as variation in chamber pressure, alignment, electrolyte film thickness, and inhomogeneity of the electrolyte film. Below, we will show that such non-idealities can be analyzed and corrected using the combination of Au 4f (electrode), O 1s from H_2O_{liq} (O $1s_{liq}$, bulk electrolyte), and K 2p (ion) spectra, combined with SESSA modeling. The first step in this procedure is to correct the effects of chamber pressure and alignment variation. This can be done using the O $1s_{liq}$ intensity, which is unaffected by the applied potential and electrolyte film thickness within our experimental range (see Fig. 6a), and therefore reflects only the effects of alignment/chamber pressure variation. Alignment/pressure-corrected K 2p and Au 4f spectra can therefore be obtained by normalizing to the corresponding O $1s_{liq}$ intensity. As shown in Fig. 6d, this correction has a modest but observable effect on the signal-to-noise in our K 2p trend.

Another source of non-ideality could be that the electrolyte film is not homogeneous over the measurement spot and that this inhomogeneity changes as a function of potential. In Fig. 6b, we modeled several inhomogeneity scenarios that would lead to the same Au 4f attenuation and would therefore go unnoticed in our Au 4f attenuation analysis. For most cases, Fig. 6b shows that the variation in electrolyte film inhomogeneity hardly impacts the K 2p signal. Only completely dry surface patches would distort the K 2p signal. We believe this was not the case in our experiments, because such dry patches would contain accumulated dry residual $KClO_4$ after the dip and pull procedure. Dry salts would produce a strong, unattenuated K 2p signal that would not exhibit a BE shift with applied potential since no longer part of the electrolyte. Since neither an unattenuated K 2p contribution nor a

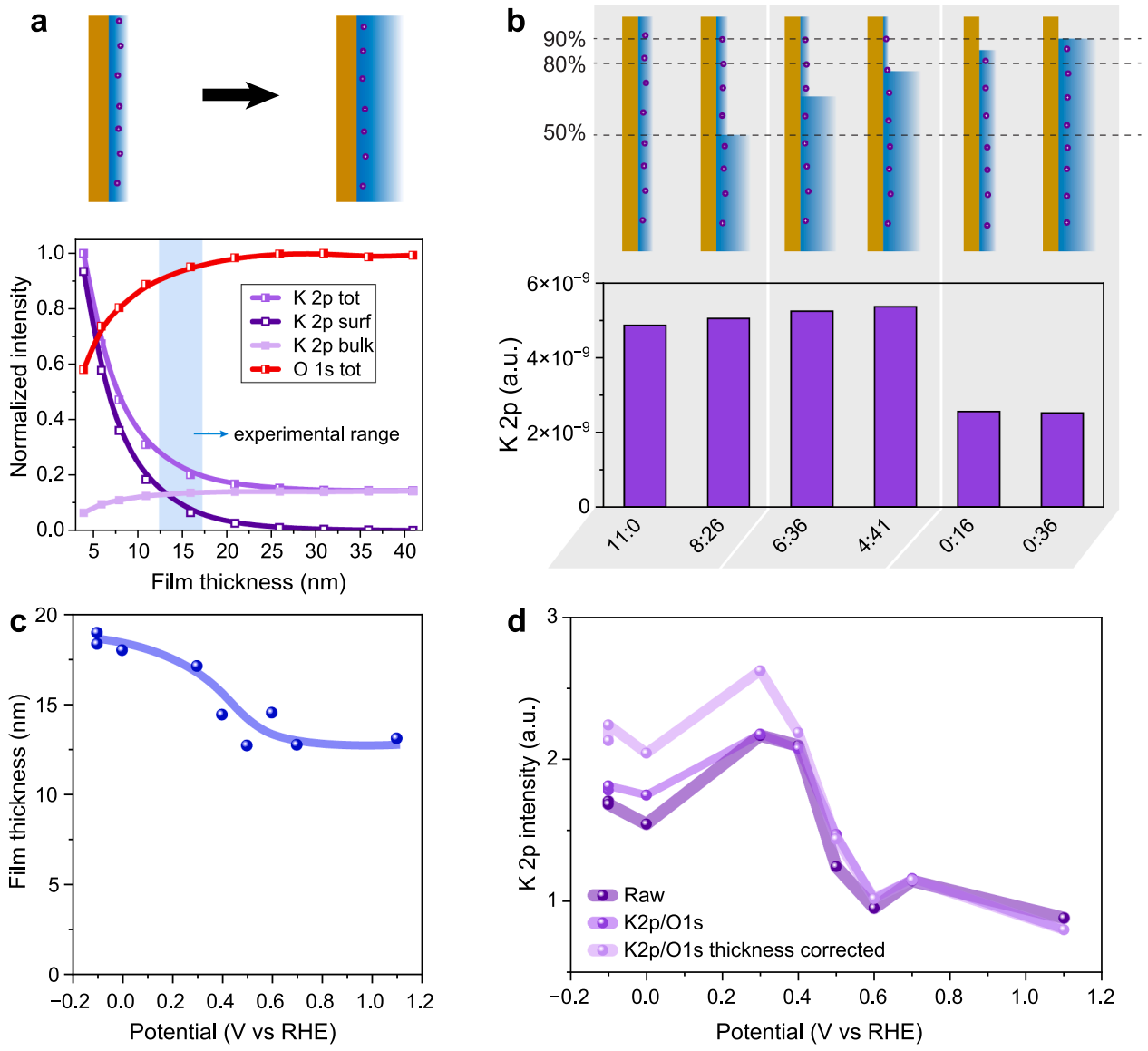

Fig. 6. Modeling of electrolyte film thickness effects on the K 2p/Au 4f signal. (**a**) Electrolyte film thickness effect on the modeled K 2p intensities from the surface, the bulk, and both, normalized by K 2p total intensity, and on the modeled O 1s intensity normalized by O 1s total intensity. The range of film thickness observed experimentally is highlighted in blue. (**b**) Theoretical K 2p intensity simulated with SESSA for a rough electrode surface in 6 different scenarios of electrolyte film thickness distribution, each corresponding to the Au 4f attenuation of a 10 nm homogeneous film. The system is modeled for $C_{bulk} = 50$ mM and $\langle C_{dl} \rangle = 2$ M. (**c**) Electrolyte film thickness as a function of potential determined with SESSA from the experimental Au 4f assuming a rough electrode surface. (**d**) Comparison of the raw, O 1s normalized, and film thickness corrected K 2p intensities as a function of the applied potential. Each dataset is normalized by the bulk intensity estimated as the average of the 3 most positive potentials, i.e., in and positive of the PZC region.

potential-independent component is observed in our spectra, dry salt artifacts can be excluded, indicating that the measurement area is largely covered by electrolyte. Overall, our analysis thus shows that the K 2p trend as a function of potential genuinely reflects changes in the interfacial K^+ ion concentration but can be made more accurate by appropriate correction for alignment, chamber pressure, and electrolyte film thickness variation. This also emphasizes the importance of systematically checking for non-linear potential-dependent BE shifts [14–16].

With the optimized K 2p data, we now analyze the behavior of K^+ ions in the double layer by comparing the XPS data to results from the modified Poisson-Boltzmann model and AIMD simulations. First, we analyze the K 2p intensity variation in Fig. 7. The region of PZC is readily extracted from the data as the lowest potential where the K 2p intensity reaches its minimum value, i.e., where the K^+ ions are no longer attracted to the double layer. This occurs at 0.5–0.7 $V_{RHE,}$ which corresponds to a PZC region in good agreement with the literature [37, 38]. Considering the roughened polycrystalline nature of the Au electrode, the measured minimum does not correspond to this surface's true PZC, but rather, to the average contributions from the PZC of different coexisting Au orientations. This *apparent* PZC measured by EC-XPS seems to agree best with the model when using a PZC = 0.7 V_{RHE}.

The second aspect that can be analyzed from the K 2p intensity is the potential dependence of the interfacial ion concentration. As can be seen in Fig. 7, K^+ ions are attracted to the electrode when the potential is moved below the PZC region, and the cation signal increases at more negative potentials. However, the signal levels off at ~0.3 V_{RHE}, suggesting a reduced increase in the interfacial K^+ concentration at more negative potentials. This trend is reproduced by the modified Poisson-Boltzmann model. As shown in **Fig. S16**, this leveling-off likely reflects a reduced capacitance caused by saturation of the orientational polarization of water molecules [22], i.e., the reduction of the dielectric

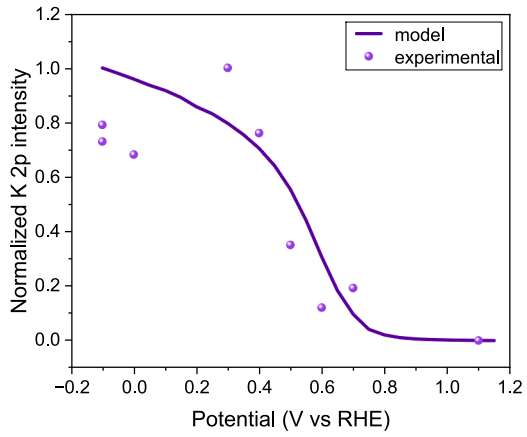

Fig. 7. Determination of the local K^+ cations concentration in the double layer by fitting the EC-XPS with a modified Poisson-Boltzmann model. Comparison of the experimental (spheres) film thickness corrected K 2p intensity as a function of the applied potential with that predicted by the Poisson-Boltzmann model in combination with a straight-line approximation for the attenuation in the liquid (line). The dependence of these results on the exact parameter choices made in the model is shown in **Fig. S11**. The simulated intensities were scaled such that the predicted intensity at 1 V vs. RHE (a potential considerably above the set PZC) matches the mean measured intensity obtained at the 3 most positive potentials. Experimental and modeled data are normalized between 0 and 1 using their respective minimum and maximum.

response at the interface due to a strong local electric field. We chose to compare the normalized model-derived and experimental K 2p data here because converting experimental data into absolute ion concentrations is challenging. While it is theoretically possible to establish an absolute scale using the K 2p intensity above PZC, which corresponds to the bulk 50 mM concentration (no K^+ accumulation in the EDL), this approach is likely unreliable. This conversion would be inaccurate due to (1) noise in the signal and (2) perturbations of the "bulk" concentration from the possible contribution of ion accumulation at the gas-liquid interface.

Apart from the K 2p signal intensity, we can also analyze the potential experienced by the interfacial K^+ ions using the K 2p peak position. In the double layer, the electrostatic potential transitions from 0 at the (grounded) electrode to the value for the bulk electrolyte, as schematically depicted in Fig. 3a. EDL ions located within this potential decay region will therefore experience a BE shift smaller than that of the bulk electrolyte. However, the K 2p signal is found to shift by −1.03 ±0.14 eV/V (Fig. 8a), i.e. the BE shift is equal to the −1 eV/V expected for the bulk electrolyte. Indeed, the shift is very similar to that of the bulk-dominated O $1s_{liq}$ peak (remaining differences are within the measurement uncertainty). This suggests that the potential decay through the double layer mainly occurs close to the Au surface in a region that is not accessed by (large amounts of) ions. Further confirmation for this comes from analysis of the peak width (FWHM) of the K 2p data. If double layer ions experience a different BE shift than ions in the bulk of the electrolyte, the K 2p peak would broaden. However, as shown in **Fig. S18**, no significant broadening is observed.

The potential presence of a rapid potential decay at the interface has been discussed based on AIMD and density functional theory calculations in the work of Zhu et al. [48]. Our modified Poisson-Boltzmann model also suggests such a rapid potential decay (see Fig. 8c), which largely occurs in the region close to the electrode surface where no ions are present yet. Fig. 8b shows that as a result of this, the ions should indeed exhibit a BE shift close to that of the bulk ions (−0.83 eV/V. for the EDL vs. −1 eV/V for the bulk). Since the modified Poisson-Boltzmann model makes rather crude approximations and since the behavior can depend crucially on the behavior of the dielectric constant at the interface, we additionally performed AIMD simulations and tracked the potential shift experienced by the individual ions via the 3s peak in the projected density of states (results for the 3p peak are shown in **Fig. S19**).

As shown in Fig. 8d the AIMD simulations also indicate that the EDL ions residing between 3 Å and 6 Å experience nearly the same electrostatic potential: In this range, we find a potential shift of only about 0.12 eV, much smaller than the potential applied. Given additionally the strongly localized ion distribution suggested by our simulations to occur at −1.26 V vs. PZC (see **Fig. S20**), these results clearly support that a steep potential drop is present in the first molecular layer near the electrode's surface, as already suggested by the modified Poisson-Boltzmann model. This suggests that even ions in closest proximity to the electrode experience only a small potential difference relative to bulk ions. In other words, although part of the EDL, the charge screening of these ions is mediated by interfacial water molecules that "buffer" the potential the cations experience. Our analysis thus highlights the effectiveness of potential screening in the double layer at potentials far from PZC, even at a modest ion concentration of 50 mM.

4. Conclusion

Overall, our work highlights how EC-XPS in the dip-and-pull geometry is an effective, semi-quantitative methodology for the study of interfacial ion behavior. Key double layer parameters, such as the PZC, interfacial ion concentrations, and the potential experienced by ions in the EDL can be directly accessed or estimated from the XPS spectra of ion core levels as a function of applied potential. Caution is necessary, though, as we note that these extracted parameters can be readily perturbed by variations in electrolyte film thickness, lack of (full) electrochemical contact, and dry spots on the surface. Accordingly, ensuring reproducible and complete electrode wetting, as well as applying appropriate corrections for remaining electrolyte film variations, is crucial to attain reliable data. Key points in the methodology presented here, therefore, are the practical indicators and corrections used in the data analysis that ensure that meaningful insight is extracted.

After validating our data with these indicators and corrections, we have analyzed the case study of the Au-50 mM $KClO_4$ interface. We find a PZC in the range of 0.5–0.7 V_{RHE}, in agreement with the literature. Moving to more negative potentials, K^+ ions are readily attracted to the interface. Based on our data, we find a decrease in capacitance occurring already at ~0.3 V_{RHE} (~0.4 V lower than PZC). Using a modified Poisson-Boltzmann model, we find the capacitance decrease (and hence slower cation signal increase) to be caused by dielectric saturation effects. Finally, our data suggests that despite the modest ion concentration used here, the electrolyte is extremely effective in screening the potential applied to the electrode, with most of the potential drop already occurring in or below the first water layer. Thus, our EC-XPS data provides direct atomic-scale insight, both in terms of structure and potential. We anticipate that such insight will provide useful guidance for understanding the charging mechanisms of supercapacitors and electrolyte effects in electrolysis.

CRediT authorship contribution statement

Sheena Louisia: Writing – review & editing, Writing – original draft, Visualization, Validation, Project administration, Methodology, Investigation, Funding acquisition, Formal analysis, Data curation, Conceptualization. **Jordy J.J. Eggebeen:** Writing – review & editing, Validation, Investigation, Formal analysis. **Ariba Adnan:** Writing – review & editing, Validation, Investigation. **Nipon Deka:** Validation, Investigation. **Lucas B.T. de Kam:** Writing – review & editing, Visualization, Methodology, Investigation, Formal analysis, Data curation. **Kees E. Kolmeijer:** Validation, Investigation. **Nicci L. Fröhlich:** Writing – review & editing, Validation, Investigation. **Rick S. Kort:** Writing – review & editing, Visualization, Methodology, Investigation, Formal analysis. **Katharina Doblhoff-Dier:** Writing – review & editing, Visualization, Supervision, Resources, Project administration,

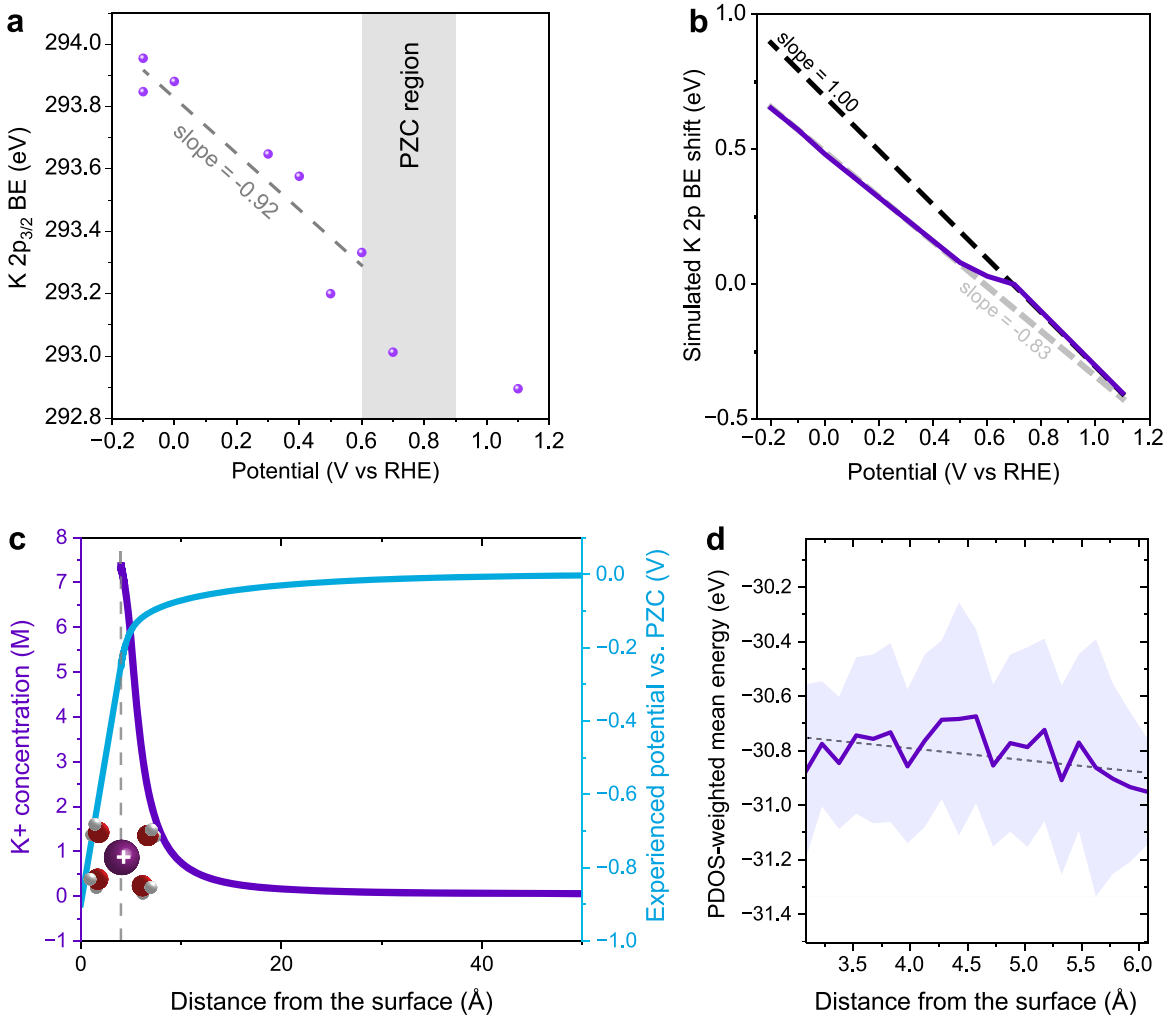

Fig. 8. Potential effect on the binding energy of EDL ions. (a) K $2p_{3/2}$ BE (spheres) as a function of the applied potential corresponding to the K 2p spectra in Fig. 5b fits a linear function (grey dotted line) of −1.03±0.14 eV/V. **(b)** Simulated BE shift of K 2p photoelectrons as a function of applied potential estimated from the modified Poisson-Boltzmann model exhibits a slope of −0.83 eV/V (grey dotted line) below the PZC = 0.7 V vs RHE. **(c)** Most of the potential drop experienced by most cations occurs in the first 1 nm from the surface. The solvated K^+ are estimated at 4 Å according to other AIMD calculations[23]. **(d)** PDOS-weighted mean energy of the K^+ s states, relative to the instantaneous Fermi level, as a function of distance to the surface, obtained from AIMD simulations. Purple line: average over all ions within each distance bin. Shaded area: standard deviation of the mean. The dashed black line indicates a linear fit with a slope of −0.04 eV/Å.

Methodology, Formal analysis, Data curation. **Ethan J. Crumlin:** Validation, Supervision, Resources, Investigation, Formal analysis, Data curation. **Marc T.M. Koper:** Writing – review & editing, Supervision, Resources, Project administration, Funding acquisition, Conceptualization. **Rik V. Mom:** Writing – review & editing, Writing – original draft, Visualization, Validation, Supervision, Resources, Project administration, Methodology, Investigation, Funding acquisition, Formal analysis, Data curation, Conceptualization.

Declaration of competing interest

The authors declare that they have no known competing financial interests or personal relationships that could have appeared to influence the work reported in this paper.

Acknowledgments

We thank the Advanced Light Source (ALS) for the provision of synchrotron radiation facilities at beamline 9.3.1.1. (proposal ID ALS-12249). We thank Dr. Rebecca Hamlyn, Dr. Johannes Mahl, and Dr. Haoyi Li for their help and support at beamline 9.3.1. This research used resources of the Advanced Light Source, which is a DOE Office of Science User Facility under contract no. DE-AC02-05CH11231. S.L acknowledges funding from 2022 HORIZON-MSCA-PF program under grant agreement No 101109314 and the Leiden University Fund (LUF). S.L., J. E., A.A., N.L.F., and M.T.M.K. also received funding from the European Research Council (ERC) (Advanced Grant no. 101019998 "FRUMKIN"). R.V.M and N.D. acknowledge the Dutch Organization for Scientific Research (NWO) for funding under grant number ECCM.TT.001. K.D.D., R.S.K and L.B.T.K acknowledge that this publication is part of the project "Computational Electrochemistry" with file number 2025.014 of the research programme "Computing Time on National Computer Facilities" which is (partly) financed by the Dutch Research Council (NWO) under the grant https://doi.org/10.61686/BOKDD81349. E.J.C. was partially supported by the Condensed Phase and Interfacial Molecular Science Program (CPIMS), in the Chemical Sciences Geosciences and Biosciences Division of the Office of Basic Energy Sciences of the U.S. Department of Energy under Contract No. DE-AC02-05CH11231.

Supplementary materials

Supplementary material associated with this article can be found, in the online version, at doi:10.1016/j.electacta.2026.149132.

Data availability

Data will be made available on request.

References

[1] P. Li, et al., Hydrogen bond network connectivity in the electric double layer dominates the kinetic pH effect in hydrogen electrocatalysis on Pt, Nat. Catal. 5 (2022) 900–911.

[2] P. Li, et al., Revealing the role of double-layer microenvironments in pH-dependent oxygen reduction activity over metal-nitrogen-carbon catalysts, Nat. Commun. 14 (2023).

[3] P. Sebastián-Pascual, Y. Shao-Horn, M. Escudero-Escribano, Toward understanding the role of the electric double layer structure and electrolyte effects on well-defined interfaces for electrocatalysis, Curr. Opin. Electrochem. 32 (2022), https://doi.org/10.1016/j.coelec.2021.100918. Preprint at.

[4] Z.M. Zhang, et al., Probing electrolyte effects on cation-enhanced CO2 reduction on copper in acidic media, Nat. Catal. 7 (2024) 807–817.

[5] A. Auer, F.J. Giessibl, J. Kunze-Liebhäuser, Combining electrochemical scanning tunneling microscopy with force microscopy, ACS nano 19 (9) (2025) 8401–8410, https://doi.org/10.1021/acsnano.5c00591.

[6] M. Favaro, et al., Elucidating the alkaline oxygen evolution reaction mechanism on platinum, J. Mater. Chem. Mater. 5 (2017) 11634–11643.

[7] H. Javed, et al., The potential-dependent structure of Pt3Ni alloy electrocatalysts and its effect on electrocatalytic activity, ACS Catal. 15 (2025) 12994–13002.

[8] M. Favaro, et al., Unravelling the electrochemical double layer by direct probing of the solid/liquid interface, Nat. Commun. 7 (2016).

[9] S. Zhao, Y. Yang, Z. Tang, Insight into structural evolution, active sites, and stability of heterogeneous electrocatalysts, Angew. Chem. Int. Ed. 61 (2022), https://doi.org/10.1002/anie.202110186. Preprint at.

[10] H. Javed, et al., A laboratory-based electrochemical NAP-XPS system for operando electrocatalysis studies, Vacuum 231 (2025).

[11] C. Griesser, et al., Lab-based electrochemical X-ray photoelectron spectroscopy for in-situ probing of redox processes at the electrified solid/liquid interface, in: Electrochemical Science Advances, 4, 2024.

[12] R.V. Mom, et al., Operando structure-activity-stability relationship of iridium oxides during the oxygen evolution reaction, ACS Catal. 12 (2022) 5174–5184.

[13] S. Axnanda, et al., Using 'tender' X-ray ambient pressure X-ray photoelectron spectroscopy as A direct probe of solid-liquid interface, Sci. Rep. 5 (2015).

[14] C. Arble, et al., Radiation damage of liquid electrolyte during focused X-ray beam photoelectron spectroscopy, Surf. Sci. 697 (2020) 121608.

[15] S.H. Cheng, C.H. Chang, J.J. Velasco-Velez, B.H. Liu, Soft X-ray induced radiation damage in dip-and-pull photon absorption and photoelectron emission experiments, J. Phys. Chem. C 128 (2024) 14381–14387.

[16] W. Bras, D.A.A. Myles, R. Felici, When x-rays alter the course of your experiments, J. Phys. Condens. Matter. 33 (2021), https://doi.org/10.1088/1361-648X/ac1767. Preprint at.

[17] Werner, W.S.M., Smekal, W. & Powell, C.J. *Simulation of electron spectra for surface analysis (SESSA) version 2.1 User's guide*. (2016) doi:10.6028/NIST.NSRDS.100-2017.

[18] A. Abrashkin, D. Andelman, H. Orland, Dipolar Poisson-Boltzmann equation: ions and dipoles close to charged surfaces. , 2007, https://doi.org/10.1103/PhysRevLett.99.077801.

[19] A. Iglič, E. Gongadze, V. Kralj-Iglič, Differential capacitance of electric double layer – Influence of asymmetric size of ions, thickness of stern layer and orientational ordering of water dipoles, Acta Chim. Slov. 66 (2019) 534–541.

[20] E. Gongadze, A. Iglič, Decrease of permittivity of an electrolyte solution near a charged surface due to saturation and excluded volume effects, Bioelectrochemistry 87 (2012) 199–203.

[21] B.E. Conway, M. Bockris, I.A. Ammar, The dielectric constant of the solution in the diffuse and Helmholtz double layers at a charged interface in aqueous solution, Trans. Farad. Soc. (1951) 756–766.

[22] E. Zhen, Y. Chen, J. Huang, Double-layer capacitance peaks: origins, ion dependence, and temperature effects, J. Chem. Phys. 162 (2025).

[23] Guo, J., Calegari Andrade, M., Hahn, C., Kulkarni, A. & Govindarajan, N. Understanding cation and surface charging effects at electrified interfaces using neural network interatomic potentials. Preprint at https://doi.org/10.26434/chemrxiv-2025-076cz-v2 (2025).

[24] L.B.T. de Kam, frumkin: Modelling of electrified interfaces using Poisson-Boltzmann theory. github.com/lucasdekam/frumkin, 2025 last commit f423573 on October 20, 2025.

[25] *Introduction to solid State physics Charles Kittel*. (2005).

[26] J. Vandevondele, et al., Quickstep: fast and accurate density functional calculations using a mixed Gaussian and plane waves approach, Comput. Phys. Commun. 167 (2005) 103–128.

[27] Goedecker, S., Teter, M. & Hutter, J. *Separable dual space Gaussian pseudo-potentials*.

[28] B. Hammer, L.B.L.B. Hansen, J.K.J.K. Nørskov, Improved adsorption energetics within density-functional theory using revised Perdew-Burke-Ernzerhof functionals, Phys. Rev. B Condens. Matter. Mater. Phys. 59 (1999) 7413–7421.

[29] S. Grimme, Semiempirical GGA-type density functional constructed with a long-range dispersion correction, J. Comput. Chem. 27 (2006) 1787–1799.

[30] T.D. Kühne, M. Krack, F.R. Mohamed, M. Parrinello, Efficient and accurate car-parrinello-like approach to born-oppenheimer molecular dynamics, Phys. Rev. Lett. 98 (2007).

[31] L.M. Liu, M. Krack, A. Michaelides, Interfacial water: a first principles molecular dynamics study of a nanoscale water film on salt, J. Chem. Phys. 130 (2009).

[32] J.B. Le, et al., Modeling electrified Pt(111)-Had/water interfaces from Ab Initio Molecular dynamics, JACS Au. 1 (2021) 569–577.

[33] W.L. Jorgensen, J. Chandrasekhar, J.D. Madura, R.W. Impey, M.L. Klein, Comparison of simple potential functions for simulating liquid water, J. Chem. Phys. 79 (1983) 926–935.

[34] H. Heinz, R.A. Vaia, B.L. Farmer, R.R. Naik, Accurate simulation of surfaces and interfaces of face-centered cubic metals using 12-6 and 9-6 lennard-jones potentials, J. Phys. Chem. C 112 (2008) 17281–17290.

[35] I.S. Joung, T.E. Cheatham, Determination of alkali and halide monovalent ion parameters for use in explicitly solvated biomolecular simulations, J. Phys. Chem. B 112 (2008) 9020–9041.

[36] J. Le, M. Iannuzzi, A. Cuesta, J. Cheng, Determining potentials of zero charge of metal electrodes versus the standard hydrogen electrode from density-functional-theory-based Molecular dynamics, Phys. Rev. Lett. 119 (2017).

[37] S. Strbac, R.R. Ad&c, A. Hamelin, Oxide formation on gold single crystal stepped surfaces, J. Electroanal. Chem. 249 (1988).

[38] A. Hamelin, Lausanne-printed in the netherlands the crystallographic orientation of gold surfaces at the gold-aqueous solution interphases, J. Electroanal. Chem. 142 (1982).

[39] H. Shinotsuka, et al., Calculations of electron inelastic mean free paths. XI. Data for liquid water for energies from 50 eV to 30 keV, Surf. Interf. Anal. 49 (2017) 238–252.

[40] Fadley, C.S. *Surface Analysis, Peak Intensities and Angular Distributions in XPS*. vol. 2 (1975).

[41] Holloway, P.H. *The effect of surface roughness on Auger electron spectroscopy*.

[42] P.L.J. Gunter, O.L.J. Gijzeman, J.W. Niemantsverdriet, Surface roughness effects in quantitative XPS: magic angle for determining overlayer thickness, Appl. Surf. Sci. 115 (1997) 342–346.

[43] J.J. Velasco-Velez, et al., A comparative study of electrochemical cells for in situ x-ray spectroscopies in the soft and tender x-ray range, J. Phys. D. Appl. Phys. 54 (2021).

[44] D. Teschner, et al., Understanding anomalous gas-phase peak shifts in dip-and-pull ambient pressure XPS experiments, J. Phys. Chem. C 128 (2024) 7096–7105.

[45] A.M. Gómez-Marín, A. Boronat, J.M. Feliu, Electrocatalytic oxidation and reduction of H2O2 on Au single crystals, Russ. J. Electrochem. 53 (2017) 1029–1041.

[46] P.S. Germain, W.G. Pell, B.E. Conway, Evaluation and origins of the difference between double-layer capacitance behaviour at Au-metal and oxidized Au surfaces, Electrochim. Acta 49 (2004) 1775–1788.

[47] A. Adnan, S. Behjati, N. Félez-Guerrero, K. Ojha, M.T.M. Koper, Tracking the surface structure and the influence of cations and anions on the double-layer region of a Au(111) electrode, Phys. Chem. Chem. Phys. 26 (2024) 21419–21428.

[48] J.X. Zhu, J. Cheng, K. Doblhoff-Dier, Dielectric profile at the Pt(111)/water interface, J. Chem. Phys. 162 (2025).